Key Points:

- The interaction of the spatial-mean tide with rough bathymetry generates baroclinic motion including internal tides
- These motions exert stresses on the spatial-mean tide near the seafloor which modifies the benthic tidal amplitude
- The benthic tidal amplitude may be decreased or increased depending on the nature of the interaction

Correspondence to:
C. J. Shakespeare,
callum.shakespeare@anu.edu.au

The Impact of Abyssal Hill Roughness on the Benthic Tide

Callum J. Shakespeare[1] , **Brian K. Arbic**[2] , and **Andrew McC. Hogg**[1]

[1]Research School of Earth Sciences, ARC Centre of Excellence in Climate Extremes, Australian National University, Canberra, ACT, Australia, [2]Earth and Environmental Sciences, University of Michigan, Ann Arbor, MI, USA

Abstract The flow of tides over rough bathymetry in the deep ocean generates baroclinic motion including internal waves and bottom-trapped tides. The stresses generated by this motion feedback on the amplitude and phase of the large-scale tide. Quantifying the stresses associated with tidal flow over abyssal hills is especially important, as this scale of bathymetry is often unresolved in global baroclinic tide models, and the stresses must therefore be parameterized. Here, we extend the previous theoretical work of the authors to determine the amplitude, phasing, and vertical location of the stresses exerted on a flow driven by a time-periodic body force when it encounters rough bathymetry. The theory compares favorably with a suite of fully nonlinear numerical simulations. It is shown that all topographic stresses are applied directly above the bathymetry, leading to a two-layer baroclinic flow, with the near-bottom spatial-mean flow (the benthic tide) strongly modified by topographic stresses, and the flow at height unperturbed by the presence of topography. Our results provide a framework to improve baroclinic tide models by (i) providing a simple parameterization for the subinertial stress which is currently not included in any models, (ii) establishing that parameterized stresses should be applied in the diffusive boundary layer directly above the topography, independent of where internal tides may dissipate, and (iii) identifying a minimum resolution of ~10 km for baroclinic tidal models to adequately capture wave resonance effects that can significantly impact the magnitude of the benthic tide.

Plain Language Summary The ocean tide is a periodic motion of the water column at the scale of ocean basins. The amplitude of the ocean tide is determined by a balance between the gravitational attraction of the moon and the forces exerted when the tide flows over the rough seafloor. Much of the roughness in the deep ocean is due to mountains on the seafloor, 10–50 km in width, known as "abyssal hills." In this study, mathematical descriptions are developed for the strength and distribution of the forces exerted on the ocean tide due to its interaction with these hills. These forces always act below the crest of the hills, leading to a sub-crest or "benthic tide" that differs from the tide above the crest of the hills. Our results provide a framework for improving the representation of tides in numerical ocean models.

1. Introduction

The ocean tides are driven by time-periodic body forces resulting from the variable gravitational attraction of the sun and moon at a fixed point on the rotating Earth. The forces are uniform over the ocean depth and thus, in a flat-bottomed, frictionless "bathtub" ocean, would drive a depth-invariant, time-periodic flow at the 1,000–10,000 km scales of ocean basins (e.g., Egbert & Erofeeva, 2002). However, the ocean bottom is not flat, with 100–1,000 km scale bathymetry such as mid-ocean ridges and continental shelves, and ubiquitous 1–100 km scale mountains in the deep ocean known as "abyssal hills" (Goff, 1991, 2010; Goff & Arbic, 2010; Goff & Jordan, 1988). At the scale of these abyssal hills, the astronomical body forcing that drives the tide is horizontally and vertically uniform, and therefore so is the flow in the absence of these hills. However, the addition of the bathymetry generates motion at the horizontal scales of the hills including internal waves (e.g., Bell, 1975), bottom turbulence (e.g., Winters & Armi, 2014), and bottom-trapped tides (Falahat & Nycander, 2015). These flows can exert stresses (e.g., wave drag) that modify the horizontally averaged tidal flow. Here we seek to quantify these stresses and their impact on the deep ocean tide.

Shakespeare et al. (2020, hereafter, SAH) developed a theoretical model to address this question. They investigated the impact of rough topography on the horizontally and vertically averaged mean flow in the

presence of a spatially uniform, time-periodic body forcing. The interaction of the mean flow with topography was shown to induce two types of stresses on the mean flow: a "wave drag" associated with radiating internal waves, and a "spring force" associated with both internal waves reflecting off the ocean surface and subinertial, bottom-trapped tides. The term "spring force" was adopted to describe this latter stress because it is analogous to the force generated by the spring in a classical forced-damped harmonic oscillator; that is, the force is out-of-phase with the velocity of the oscillating mass (tidal flow) and absorbs and releases energy over the period of the motion, without extracting any net energy from the oscillator. By contrast, wave drag forces are in phase with the tidal velocity and always extract energy from the system, in this case, through the energy flux of the radiating internal waves. Prior to SAH, previous models of stresses due to topographic interactions (e.g., Bell, 1975; Garner, 2005; Green & Nycander, 2013; Jayne & St. Laurent, 2001) had only described the wave drag and had omitted the spring force. The SAH model further showed that the magnitude and type of stress exerted by internal-tide-generating bathymetry depends on the dissipation of the internal tides. SAH considered the two limits of strong and weak dissipation. For strong dissipation, the internal waves do not reflect and thus exert only the wave drag force. For vanishingly weak dissipation, the waves exert both a drag force and a spring force associated with the reflections. SAH derived simplified forms for the vanishing dissipation limit under a number of simplifying assumptions about the topographic spectrum but did not consider arbitrary levels of dissipation.

The SAH model is a depth-averaged (barotropic) model. In other words, it is assumed that the depth-mean tidal flow interacts with the bathymetry and generates baroclinic motion. This assumption is unlikely to be valid since the horizontally averaged tidal flow will vary in the vertical depending on where and what topographic stresses are applied. For example, if a wave drag is applied at (or just above) the bathymetry, we might expect the near-bottom tidal flow to be smaller than the tidal flow at height. Since it is this near-bottom tidal flow that subsequently interacts with the bathymetry to generate further motion (e.g., internal waves) and associated stresses, this effect will result in feedback in the system, and the resulting stresses will differ from those that would be generated if the depth-mean flow itself interacted with the bathymetry (e.g., Kelly et al., 2010; Kelly & Nash, 2010). Thus, an understanding of the vertical location at which topographic stresses (both wave drag and spring forces) are applied is important, but currently lacking.

In recent years, astronomical tidal forcing has been implemented in a global high-resolution ocean general circulation models, beginning with simulations of HYCOM (Arbic et al., 2010, 2012), and now including simulations of MITgcm (Arbic et al., 2018; Rocha et al., 2016) and MOM6 (Adcroft et al., 2019). Such models are being used for many different applications including as preparations for the SWOT satellite mission (Wang et al., 2018) and to generate boundary conditions for regional models (Nelson et al., 2020). The amplitudes of both the barotropic and baroclinic tides in such models are sensitive to the parameterized drag schemes employed (e.g., Ansong et al., 2015). As more modeling centers move toward including tides in high-resolution general circulation models, the need to understand the impact of small-scale, unresolved tide-topography interactions becomes greater.

Current topographic stress parameterizations in baroclinic tide models only include the wave drag force due to radiating waves (Egbert et al., 2004; Garner, 2005; Green & Nycander, 2013; Jayne & St. Laurent, 2001; Zaron & Egbert, 2006). This stress is typically applied over an arbitrary height-scale from the ocean bottom, often taken as the bottom 500 m (e.g., Ansong et al., 2015; Arbic et al., 2010). It is usually argued that the wave drag and height-scale thereof "represents the breaking of unresolved high modes...over open ocean rough topography" (Ansong et al., 2015). Thus, it is argued that the stress associated with the generation of the internal tide is applied where the waves break and dissipate. However, there is no theoretical justification for this assumed connection between the breaking of internal tides and the imposition of stress on the spatial-mean tidal flow. Instead, the argument appears to borrow from the nonacceleration theorem, which pertains to the case of a *steady* mean flow, where steady lee waves are generated, and it is well known that the lee wave stress is exerted where the waves dissipate (Andrews, 1983; Andrews & McIntyre, 1976, 1978; Boyd, 1976; Bretherton, 1969; Charney & Drazin, 1961; Eliassen & Palm, 1961; Xie & Vanneste, 2017). However, it has been shown that this theorem need not apply to lee wave generation in transient flows (e.g., Bölöni et al., 2016), and thus its application to an oscillatory (tidal) mean flow is questionable.

The study is laid out as follows. In Section 2, we present a summary of the SAH theory and its extension to include the vertical structure of topographic stress. It is shown that, while the topographic stress is indeed

applied immediately above the topography, it is not related to the location of dissipation of the internal tide. Section 3 describes the configuration of a suite of numerical simulations in MITgcm to test the extended theory. The results of the simulations and comparison with the theory are presented in Section 4. In Section 5, we assess the utility of these results in developing improved stress parameterizations for baroclinic tidal models. We argue that while neglecting the spring forces associated with internal wave reflections (as is currently done) is not unreasonable, it is essential that the spring forces associated with bottom-trapped tides, in addition to propagating internal wave drag, are incorporated in future topographic stress parameterizations. We conclude in Section 6.

2. Theory

SAH developed a barotropic model for the impact of topographic stresses on the spatial-mean time-periodic flow; that is, a model with velocities averaged over the full ocean depth. In this section, we investigate where the topographic stresses are applied, and use this knowledge to construct an extended model to capture the depth-dependent structure of the spatial-mean time-periodic flow. Here, we examine a quasi-2D system (uniform in the y direction), consistent with the numerical model to be used in Section 3, but we note that the results are readily generalizable to the fully 3D case using the 3D expressions from SAH.

2.1. Where are Time-Periodic Topographic Stresses Applied?

The quasi-2D rotating fluid equations linearized about some spatial-mean periodic flow $(U(t), V(t), 0)$ in the Cartesian (x, y, z) directions, and background buoyancy $B = N^2(z + H)$ (where $z = -H$ is the mean depth of the ocean bottom), subject to a purely periodic body force $F(t) = F_0 \sin \omega t$ in the x-direction, are

$$Du - fv = -\frac{\partial p}{\partial x} + F + \kappa \nabla^2 u, \tag{1a}$$

$$Dv + fu = \kappa \nabla^2 v, \tag{1b}$$

$$Dw = -\frac{\partial p}{\partial z} + b' + \kappa \nabla^2 w, \tag{1c}$$

$$Db' + wN^2 = \kappa \nabla^2 b', \tag{1d}$$

$$\frac{\partial u}{\partial x} + \frac{\partial w}{\partial z} = 0, \tag{1e}$$

where the linearized material derivative is

$$D = \frac{\partial}{\partial t} + U \frac{\partial}{\partial x}, \tag{1f}$$

(u, v, w) is the total velocity, b the total buoyancy, p the dynamic pressure, and κ the diffusivity/viscosity. The total fields (e.g., u, v, b) are composed of background (e.g., U, V, B) and perturbation (e.g., u', v', b') components such that $u = U + u'$, $v = V + v'$, etcetera. Here, the body force F represents the "effective body force" associated with the barotropic tide in the absence of topography; that is, $F = -g\partial_x\eta(x, t)$, where $\eta(x, t)$ is a tidal surface elevation in the absence of topography. Thus, F may differ from the astronomical forcing, owing to large-scale basin resonances that tend to amplify the barotropic tide in certain locations.

Suppose some small-amplitude topography $h(x)$ is introduced at the bottom, where $\int_{\forall x} h(x)\, dx = 0$ such that the mean ocean depth (i.e., H) is unchanged. It follows that $w = U\partial_x h$ at the bottom, such that there is no flow through the topography. An immediate corollary from Equation 1d is that

$$(\partial_t + U\partial_x)(b' - N^2 h) = \kappa \nabla^2 b' \tag{2}$$

at the boundary. Introducing a mean-flow-following frame (x_0, z, t), where $x = x_0 + \int_0^t U(\zeta)d\zeta$ such that $h(x) = h\left(x_0 + \int_0^t U(\zeta)d\zeta\right)$, this boundary condition on the buoyancy becomes $\partial_t(b' - N^2 h) = \kappa \nabla^2 b'$, or via a Taylor expansion of $h(x)$ as

$$\partial_t b' - N^2 \partial_x h(x_0) U(t) + O(\epsilon^2) = \kappa \bar{\nabla}^2 b', \tag{3}$$

for $\epsilon = U/(\omega \Delta x) \ll 1$ (known as the small-excursion approximation). In this limit, it is clear that there are two components to the solution: a nonperiodic $O(1)$ solution, b_0, and a periodic $O(\epsilon)$ solution that scales with $U(t)$, b_1, such that $b' = b_0 + b_1$. The boundary condition on the nonperiodic solution is

$$\partial_t b_0 = \kappa \bar{\nabla}^2 b_0, \tag{4}$$

and on the periodic solution,

$$\partial_t b_1 - N^2 U \partial_x h = \kappa \bar{\nabla}^2 b_1. \tag{5}$$

Let us first consider the nonperiodic solution b_0, which is associated with the diffusive topographic boundary layer. Since $w_0 = 0$ at the boundary, and this solution is concentrated near the boundary, we will assume that $w_0 \sim 0$ throughout the fluid. It follows from Equation 1d that

$$\partial_t b_0 = \kappa \bar{\nabla}^2 b_0 \tag{6}$$

holds throughout the fluid, and not just at the boundary (i.e., Equation 4). An additional boundary condition of zero net buoyancy flux normal to the topography must also apply, or

$$\kappa(\partial_x b_0, \partial_z b_0 + N^2) \cdot (-\partial_x h, 1) = 0, \tag{7}$$

at $z = -H + h(x)$. For $\partial_x h \ll 1$ (as is always the case in geophysical settings), it follows that isopycnals are nearly flat, or $\partial_z b_0 \gg \partial_x b_0$, and thus Equations 6 and 7 may be further simplified by neglecting the horizontal derivatives:

$$\partial_t b_0 - \kappa_v \partial_{zz} b_0 = 0, \text{ where } \partial_z b_0|_{z=-H+h(x)} = -N^2. \tag{8}$$

The nonperiodic solution thus acts to cancel the background stratification near the topography. The initial condition on Equation 8 is that $\partial_z b_0$ is zero everywhere, except at the topography; that is, $\partial_z b_0 = -N^2 \delta(z - (-H + h(x)))$ at time $t = 0$, where δ is the Dirac delta function. Equation 8, subject to this initial condition, has a well-known solution:

$$\partial_z b_0 = -N^2 \left(1 - \text{erf}\left(\frac{z - (-H + h(x))}{\sqrt{4\kappa_v t}}\right)\right), \tag{9}$$

where the error function is defined by $\text{erf}(\zeta) = 2/\sqrt{\pi} \int_0^\zeta e^{-\gamma^2} d\gamma$. The corresponding horizontal buoyancy gradient (which will be needed below) is

$$\partial_x b_0 = -N^2 \partial_x h \left(1 - \text{erf}\left(\frac{z - (-H + h(x))}{\sqrt{4\kappa_v t}}\right)\right). \tag{10}$$

The other fields (e.g., u_0, v_0) follow from Equation 1, but are not needed here. In the small-amplitude limit, $h \ll H$, Equation 10 simplifies to

$$\partial_x b_0 = -N^2 \partial_x h \left(1 - \text{erf}\left(\frac{z + H}{\sqrt{4\kappa_v t}}\right)\right). \tag{11}$$

For the periodic solution, Equation 1 reduces to

$$\left[((\partial_t - \kappa\nabla^2)^2 + N^2)\frac{\partial^2}{\partial x^2} + ((\partial_t - \kappa\nabla^2)^2 + f^2)\frac{\partial^2}{\partial z^2}\right]b_1 = 0, \tag{12}$$

where $D = \partial_t$ in the flow-following frame. SAH calculated solutions to this equation in the weakly dissipative limit ($\kappa\nabla^2 \ll \partial_t$, or Re $= \omega/(\kappa k^2) \gg 1$ for wavenumber k and frequency ω) whereby the boundary condition (Equation 5) simplifies to $\partial_t b_1 = N^2 U \partial_x h$. The solutions are freely propagating waves for forcing frequencies $f < \omega < N$, and bottom-trapped motions for other frequencies. SAH solved the more general form of this problem including a surface boundary to obtain expressions for the wave stress—their solutions will be described below. The inclusion of the surface boundary and dissipation in this model make it distinct from prior work (e.g., Bell, 1975; Llewellyn Smith & Young, 2002). We note that our interest here is not on the dynamics of the waves themselves (which is described in a separate work; Shakespeare et al., 2021), but purely on the impact of the associated wave stresses on the spatial mean flow.

Let us now consider the equation governing the spatial-mean periodic flow. Subtracting the nonperiodic solution (i.e., b_0, v_0) from Equations 1a, 1b leaves

$$\frac{\partial u_1}{\partial t} - fv_1 = -\frac{\partial p_1}{\partial x} + F_x, \tag{13a}$$

$$\frac{\partial v_1}{\partial t} + fu_1 = 0, \tag{13b}$$

where we have neglected the viscous terms, consistent with the weak dissipation limit described previously. To obtain the equation for the spatial mean flow, we integrate the above Equation 13 in z between the ocean bottom at $z = -H + h(x)$ and a time-mean isopycnal at height $z = (B - b_0)/N^2$, and then over all $0 < x < L$, to yield

$$\frac{\partial U}{\partial t} - fV = -\frac{\tau(-H) - \tau(-H + h_0)}{h_0} + F_x, \tag{14a}$$

$$\frac{\partial V}{\partial t} + fU = 0, \tag{14b}$$

where the spatial mean flow over this volume is defined as

$$U = \frac{1}{h_0 L}\int_0^L \int_{-H+h(x)}^{(B-b_0)/N^2} u_1 \, dz \, dx, \tag{15}$$

where height $h_0 = B/N^2$ is the average height of the isopycnal above the ocean bottom (where we set $B = 0$). A similar expression applies for the spatial mean flow V. The stress profile $\tau(z)$ is given by

$$\tau(z) = \frac{1}{L}\int_0^L \frac{-b_0}{N^2}\frac{\partial p_1}{\partial x} dx = \frac{1}{L}\int_0^L p_1 \frac{1}{N^2}\frac{\partial b_0}{\partial x} dx, \tag{16}$$

for small perturbations b_0 (see SAH), where the second form is obtained via integration-by-parts. The force exerted on the fluid at a given level is the vertical divergence of this stress; that is, the change in the stress over the height of a layer, $\Delta\tau/h_0$, as per Equation 14a. Note that when $z = -H$, we have $\partial_x b_0 = -N^2\partial_x h$ from Equation 11 and thus the "usual" expression for the topographic stress is recovered.

The magnitude of the stress (Equation 16) reduces with height according to the decay of perturbations to isopycnals associated with the diffusive boundary layer above the topography (Equation 11). The height scale of this decay is $\sqrt{4\kappa_v t}$ after time t from a uniformly stratified initial condition. In reality, this scale will be set by a balance between mixing and re-stratification, with only the former represented here (and in the simulations in the next section). The key point from this analysis is that spatial-mean time-periodic stresses arise from spatial correlations of oscillatory pressure variations (p_1) with nonperiodic, slowly

varying (mean) isopycnal height gradients ($\partial_x b_0/N^2$). Thus, the time-periodic topographic stress is only applied within the diffusive boundary layer where these height gradients exist. Above the boundary layer, the stress will be zero. For a finite-amplitude topography (e.g., Equation 10), this boundary layer will span the region from the lowest point to the crest of the topography. This location at which the stress acts does not require any dissipation of the waves. As such, the generation of a time-periodic (internal tide) wave stress is distinct from the generation of a time-mean lee wave stress (which requires dissipation; i.e., the nonacceleration theorem).

2.2. A 2-Layer Flow

In order to avoid the details of the height distribution of the stress, it is convenient to introduce a two-layer model of the system. Since the stress decays with height above the bottom, as long we consider a height h_0 above the bottom that is sufficiently large (i.e., above the diffusive boundary layer), then the mean isopycnals will be flat ($\partial_x b_0 = 0$) and the stress will be zero, $\tau(-H + h_0) = 0$. However, we observe that the wave field will in general still be present at this height and drive time-dependent oscillations of the isopycnals—only the slowly varying (mean) perturbations are zero. From Equation 14, the equations governing the volumetric-mean flow below this height are simply

$$\frac{\partial U}{\partial t} - fV \quad = -\frac{\tau(-H)}{h_0} + F_x, \tag{17a}$$

$$\frac{\partial V}{\partial t} + fU \quad = 0. \tag{17b}$$

We will call the volumetric-mean flow in this near-topography layer the "benthic tide." The flow at greater heights will be unaffected by the topography and is described by the same Equation 17 but with the stress term set to zero. Note that Equation 17 are precisely the same mean flow equations obtained by SAH, but in their case, the average was taken over the full-depth ($h_0 = H$), whereas here we have split the flow into the two layers. Since here the stresses are applied over a smaller height ($h_0 \ll H$), we can expect that the impact of the stress upon the flow will be greater.

2.3. Solutions for the Benthic Tide

Following SAH, it is more convenient to write the spatial-mean tide (Equation 17) in terms of their Fourier transform in time (denoted by a hat, with $i = \sqrt{-1}$), whereby

$$-i\omega\hat{U} - f\hat{V} \quad = -\sigma\hat{U} + \widehat{F_x}, \tag{18a}$$

$$-i\omega\hat{V} + f\hat{U} \quad = 0, \tag{18b}$$

where the transform of the bottom stress has been written as $\hat{\tau}(-H) = h_0\sigma\hat{U}$ as in SAH, and σ is called the "drag coefficient" defined by

$$\sigma = \frac{1}{2\pi L h_0} \int_{-\infty}^{\infty} \frac{|\hat{h}|^2 |k|}{|\omega|} \sqrt{(N^2 - \omega^2)(\omega^2 - f^2)} \coth(imH + \gamma H) dk \tag{19}$$

(see Equation 25 in SAH). In this expression, L is the domain width, ω is the (tidal) frequency, $|\hat{h}|^2$ is the power spectrum of the topography,

$$m = \text{sgn}(\omega) |k| \sqrt{\frac{N^2 - \omega^2}{\omega^2 - f^2}}, \tag{20}$$

is the vertical wavenumber,

$$\gamma = \alpha m \frac{\omega(2N^2 - \omega^2 - f^2)}{2(N^2 - \omega^2)(\omega^2 - f^2)}, \tag{21}$$

is the wave decay rate, and

$$\alpha = A_h k^2 + A_z m^2, \tag{22}$$

is the Rayleigh drag for Laplacian viscosity (and diffusivity, assuming a Prandtl number of one) in the horizontal (A_h) and vertical (A_z) directions (e.g., Shakespeare & Hogg, 2017). Note that for a periodic domain of length L (as will be modeled in the following sections) the horizontal wavenumbers k form a discrete set, $k = 2n_x\pi/L$ for integer n_x, and thus the integral in wavenumber in Equation 19 collapses to a discrete sum:

$$\frac{1}{2\pi L}\int_{-\infty}^{\infty} dk \rightarrow \frac{1}{L^2}\sum_{n_x=-\infty}^{\infty}. \tag{23}$$

Also note that the drag coefficient (Equation 19) may be written more generically for variable stratification as

$$\begin{aligned}\sigma \;=\;& \frac{1}{2\pi L h_0}\int_{-\infty}^{\infty}\frac{|\check{h}|^2|k|}{\omega}\,\mathrm{sgn}(\omega)\sqrt{(N(-H)^2 - \omega^2)(\omega - f^2)}\\ &\coth\left(\int_{-H}^{0} im(z) + \gamma(z)dz\right)dk,\end{aligned} \tag{24}$$

where $N(-H)$ is the buoyancy frequency at the topography.

The solution for the benthic tidal flow is now straightforward to calculate from Equation 18,

$$\hat{U} = \frac{-i\omega\hat{F}_x(f^2 - \omega^2 + \mathfrak{I}[\sigma]\omega + i\omega\mathfrak{R}[\sigma])}{(f^2 - \omega^2 + \mathfrak{I}[\sigma]\omega)^2 + \omega^2\mathfrak{R}[\sigma]^2}, \quad \hat{V} = \frac{-if}{\omega}\hat{U}, \tag{25}$$

where σ has been split into its real and imaginary parts. As pointed out in SAH, the energy extracted by the topographic-induced motions is $W = \mathfrak{R}[\sigma]|\hat{U}|^2$; that is, an imaginary drag on its own extracts no energy, but can influence the spatial-mean tidal velocities as per Equation 25. For these reasons, SAH termed the imaginary component a "spring force" and the real component a "wave drag" by analogy with the archetypal forced-damped harmonic oscillator. Note that the tidal flow in the y-direction always leads the flow in x by 90° in the 2D system, and thus it is only necessary to consider the flow in x when dealing with the 2D problem (these results do not follow in 3D). Relative to the case without topography, the topographic stress causes an amplification (or decrease) of the velocities by a factor A, where

$$\begin{aligned}A \;=\;& \sqrt{\frac{(\omega^2 - f^2)^2}{(\omega^2 - f^2 - \mathfrak{I}[\sigma]\omega)^2 + \omega^2\mathfrak{R}[\sigma]^2}},\\ =\;& \sqrt{\frac{(\omega^2 - f^2)^2}{(\omega^2 - f^2)^2 - 2\mathfrak{I}[\sigma]\omega(\omega^2 - f^2) + \omega^2|\sigma|^2}}\\ \simeq\;& 1 + \frac{\mathfrak{I}[\sigma]\omega}{\omega^2 - f^2},\end{aligned} \tag{26}$$

for small $|\sigma|$, and a phase shift of

$$\begin{aligned}\tan\phi \;=\;& \frac{-\omega\mathfrak{R}[\sigma]}{\omega^2 - f^2 - \mathfrak{I}[\sigma]\omega}\\ \simeq\;& \frac{-\omega\mathfrak{R}[\sigma]}{\omega^2 - f^2},\end{aligned} \tag{27}$$

for small $\mathfrak{I}[\sigma]$. These solutions show that for small drag coefficients the change in amplitude is dominated by the imaginary part of the drag, and the change in phase is dominated by the real part. In the absence of a real

component to the drag coefficient, there is no change to the phase of the flow in the bottom layer. Furthermore, for $\Re[\sigma] > 0$ (energy extraction from the barotropic tide), the phase of the bottom layer flow will tend to *lead* the unperturbed flow (i.e., if the flow at height is $e^{-i\omega t}$, then the benthic flow is $e^{-i(\omega t - \phi)}$, which leads for $\phi < 0$). However, the amplitude may either increase or decrease depending on the sign of $\Im[\sigma]$. Following SAH, it is useful to independently consider the limits of sub-inertial ($\omega < f$) and super-inertial ($\omega > f$) forcing.

In the sub-inertial limit the stress arises from bottom-trapped nonpropagating internal tides. These tides occur poleward of the critical latitudes ($\sim 30°$ for diurnal tides) and thus this sort of stress is important for the diurnal tide (in particular) in a sizable region of the global ocean, and especially at high latitudes where the diurnal tides are dominant. As shown by SAH, in this limit the viscous dissipation has negligible impact on the solution, since bottom-trapped tidal motions naturally decay with height above the bottom. Thus, letting the decay rate $\gamma \to 0$ for $\omega < f$ in Equation 24 yields

$$
\begin{aligned}
\sigma &= \frac{1}{h_0 L^2} \frac{\sqrt{(N(-H)^2 - \omega^2)(f^2 - \omega^2)}}{|\omega|} \sum_{n_x=-\infty}^{\infty} |k||\check{h}|^2 \\
&= \frac{i}{h_0} \frac{\sqrt{(N(-H)^2 - \omega^2)(f^2 - \omega^2)}}{|\omega|} \bar{k} h_{rms}^2,
\end{aligned}
\tag{28}
$$

where $\bar{k}$ is the height-weighted mean wavenumber. From Equations 26 and 27, a larger drag coefficient (e.g., increased $N(-H)$ or h_{rms} in Equation 28) will act to reduce deep tidal velocities without changing the phase of the deep flow with respect to that at height.

In the super-inertial limit, the topographic stress arises from propagating internal tides and the viscous dissipation of these waves significantly modifies the stress. In particular, in the "strongly dissipative" limit where internal tides do not reflect back to the ocean bottom (defined by $\gamma H \to \infty$) the drag coefficient is purely real since $\coth(imH + \gamma H) \to 1$ in Equation 19 and thus:

$$
\begin{aligned}
\sigma &= \frac{1}{h_0 L^2} \frac{\sqrt{(N(-H)^2 - \omega^2)(\omega^2 - f^2)}}{|\omega|} \sum_{n_x=-\infty}^{\infty} |k||\check{h}|^2 \\
&= \frac{1}{h_0} \frac{\sqrt{(N(-H)^2 - \omega^2)(\omega^2 - f^2)}}{|\omega|} \bar{k} h_{rms}^2.
\end{aligned}
\tag{29}
$$

As noted by SAH, the form of the drag coefficient for propagating internal tides in the strongly dissipative limit (Equation 29) is identical to that for bottom trapped tides (Equation 28), but one is purely real and the other purely imaginary (due to the difference in frequencies). However, if reflections occur, then the drag coefficient for propagating internal tides also has an imaginary component (a "spring force") due to the pressures these reflecting waves exert on the topography. In both cases, the amplitude and the phase of the benthic tide will be modified. SAH only considered the strongly dissipative ($\gamma H \to \infty$) and nondissipative ($\gamma H \to 0$) limits and obtained a simplified solution in the nondissipative limit by assuming the topographic spectrum was smooth. That assumption is invalid here where we are considering a horizontally periodic domain which by nature possesses a discrete (i.e., nonsmooth) spectrum of wavenumbers. Thus, here we consider the more general case with an arbitrary level of dissipation (i.e., with σ defined by Equation 24).

3. Numerical Model

We use the MITgcm (Marshall et al., 1997) in nonhydrostatic mode to simulate a 100 km long, 3 km deep, two-dimensional (*x*-*z*) domain. The horizontal resolution is set to 97.65 m and the vertical resolution to 1.5 m. The domain is periodic in the *x*-direction. Topography is introduced based on the Goff (2010) abyssal hill spectrum for a region of the Southern Ocean; that is,

$$
|\hat{h}|^2 = 4\pi \nu h_{rms}^2 \frac{k}{k_c^2} \left(\frac{k^2}{k_c^2} + 1 \right)^{-\nu - 1}
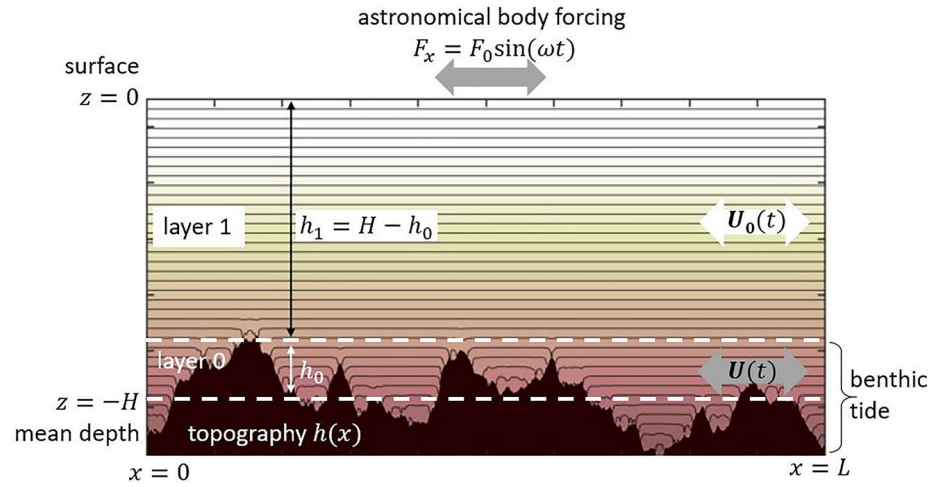\tag{30}
$$

Figure 1. Schematic of the numerical model setup. Dashed lines indicate the mean depth and the crest of the abyssal hill topography. The benthic "layer 0", which includes the diffusive boundary layer, is where all topographic forces act and runs from the deepest part of the domain to the crest of the topography. Above, in "layer 1" the spatial-mean tidal flow is unaffected by the presence of topography. The shading represents density (darker = denser) computed from the slowly evolving (mean) solution given by Equation 9 after $t = 100$ days, for $\kappa_v = 10^{-4}\ \mathrm{m^2\ s^{-1}}$, as used in the reference simulation.

where $\nu = 0.95$ is the high-wavenumber roll-off, $k_c = 1.65 \times 10^{-4}\ \mathrm{m^{-1}}$ is the cut-off wavenumber and h_{rms} (variable) is the rms height of the topography. Phases are randomly assigned to generate a physical space topography as shown in Figure 1, and thereafter, we vary the rms height by scaling the topography, while keeping the shape the same. We also introduce some runs with high- and low-pass filtered topography. The mean ocean depth is kept constant, $H = 2564\mathrm{m}$ for all runs. Body forcing is applied as a spatially uniform time-periodic acceleration in the x momentum equation such that $F_x = F_0 \sin \omega t$ in the above equations (reference value of $F_0 = 10^{-6}\ \mathrm{m\ s^{-2}}$). The flow is initialized at time zero with the velocities it would have in the absence of topography,

$$\mathbf{U}\Big|_{t=0} = \left(\frac{\omega F_0}{f^2 - \omega^2}, 0 \right). \tag{31}$$

The temperature (density) field is initialized to be horizontally uniform such that

$$\rho = \rho_0 \left(1 - \frac{1}{g} \int_{-3000}^{z} N^2 dz' \right). \tag{32}$$

Table 1
Sub-Inertial Runs: $\omega = 0.72 \times 10^{-4}\ s^{-1}$, $f = 10^{-4}\ s^{-1}$ and $A_h = 10^{-2}\ m^2 s^{-1}$

	Name	h_{rms} (m)	N^2 ($10^{-6}\ \mathrm{s^{-2}}$)	h_0 (m)	F_0 ($10^{-6}\ \mathrm{m\ s^{-2}}$)
1	Reference	100	3	222	1
2	$2h$	200	3	443	1
3	$h/5$	20	3	44	1
4	$3N$	100	27	222	1
5	$N/3$	100	0.333	222	1
6	Exponential N	100	$3(1 + 8e^{\frac{z}{500}})$	222	1
7	$2F$	100	3	222	2
8	$3F$	100	3	222	3
9	$4F$	100	3	222	4
10	$5F$	100	3	222	5

Laplacian vertical and horizontal viscosity (and diffusivity with Prandtl number of 1) are used and we set $A_z = A_h/100$. The Coriolis parameter f is fixed at $10^{-4}\ \mathrm{s^{-1}}$.

We run a suite of 27 simulations varying (i) topography rms height, (ii) stratification N^2, (iii) viscosity, (iv) forcing magnitude, and (v) forcing frequency. The parameter values for each simulation are listed in Tables 1 and 2. The two forcing frequencies chosen are the diurnal tidal frequency of $\omega = 7.2 \times 10^{-5}\ \mathrm{s^{-1}}$ (sub-inertial for the chosen f) and a frequency of approximately twice this value, $\omega = 13.889 \times 10^{-5}\ \mathrm{s^{-1}}$ (super-inertial for the chosen f)—this precise value is selected such that the flow in the absence of topography (Equation 31) is the same magnitude for both frequencies. Subinertial simulations are run for 850 h (35 tidal periods) and super-inertial simulations are run for 3,400 h (270 tidal periods) since the simulations with propagating waves take longer to equilibrate. This length of time is sufficient for the flows to develop a

Table 2
Super-Inertial Runs: $\omega = 1.3889 \times 10^{-4}\ s^{-1}$ and $f = 10^{-4}\ s^{-1}$

	Name	h_{rms} (m)	$N^2\ (10^{-6}\ s^{-2})$	h_0 (m)	A_h $(m^2\ s^{-1})$	F_0 $(10^{-6}\ m\ s^{-2})$
1	Reference	100	3	222	0.01	1
2	$2h$	200	3	443	0.01	1
3	$h/2$	50	3	111	0.01	1
4	$3N$	100	27	222	0.01	1
5	$N/3$	100	0.333	222	0.01	1
6	$3N, Ah/10$	100	27	222	0.001	1
7	$3N, 10Ah$	100	27	222	0.1	1
8	Exponential N	100	$3(1 + 8e^{\frac{z}{500}})$	222	0.01	1
9	$2h, 3N$	200	27	222	0.01	1
10	Resonant	100	3.432	222	0.01	1
11	$2F$	100	3	222	0.01	2
12	$3F$	100	3	222	0.01	3
13	$4F$	100	3	222	0.01	4
14	$5F$	100	3	222	0.01	5
15[a]	$2h$ smooth	192	3	388	0.01	1
16[b]	$2h$ rough	57	3	180	0.01	1
17[c]	$2h$ sponge	200	3	443	0.01	1

[a]Topography filtered to wavelengths exceeding 10 km.
[b]Topography filtered to wavelengths less than 10 km.
[c]10 km high domain with viscous sponge in the upper 7 km to damp reflections.

statistically steady wave field. We note that this lengthy equilibration time does not mean that it takes this length of time for the forces to act (with the exception of the stresses due to wave reflections, the forces act immediately), but rather that it takes a long time for the system to equilibrate to the imposition of the forcing, and then the subsequent feedbacks on the generation of the internal tide—waiting until this equilibrium is reached allows a cleaner comparison with the theory.

3.1. Comparison Methodology

In order to compare the numerical model results with the theory presented in the previous section, it is necessary to compute the spatial-mean flow averaged over the deep part of the model domain, up to the crest of the topography. This region includes the diffusive boundary layer and associated mean isopycnal perturbations, where the time-periodic spatial-mean stresses act (i.e., Equation 16). For example, the slowly varying (mean) solution for the buoyancy (Equation 10) is shown in Figure 1 for the numerical model parameters (i.e., $\kappa_v = 10^{-4}\ m^2\ s^{-1}$ and $h_{rms} = 100$ m) at $t = 100$ days after initialization: the corresponding height-scale of the diffusive boundary layer is $\sqrt{4\kappa_v t} = 59$m. It is apparent that essentially all mean isopycnal gradients are located within the sub-crest layer for the finite amplitude topography shown in the figure: this result will always hold when the valley-to-crest height of the topography ($\sim 2\sqrt{2}h_{rms}$) exceeds the diffusive boundary layer height (i.e., $2\sqrt{2}h_{rms} > \sqrt{4\kappa_v t}$) but may not hold for very shallow topographies.

The spatial-mean flow for each simulation is computed as the average horizontal flow over the wet part of the domain at each depth, $\bar{u}^x(z, t)$. We also wish to compute the volumetric average mean flow up to level z, which involves weighting the mean flow $\bar{u}^x(z, t)$ at each depth by the amount of area at that depth (denoted by domain length $l(z)$ in 2D), integrating, and normalizing by the total volume:

$$\bar{u}^{vol}(z, t) = \frac{\int_{-H+h}^{z} l(z')\bar{u}^x(z', t)\ dz'}{\int_{-H+h}^{z} l(z')\ dz'}. \tag{33}$$

In order to facilitate comparison with the theory for the benthic tide, we evaluate this volumetric mean flow at the crest of the topography; i.e., $U^{sim}(t) = \bar{u}^{vol}(z = -H + h_0, t)$. The amplitude and phase of this flow are then diagnosed. The amplitude is determined via $|U^{sim}| = \langle U^{sim}(t)\rangle$, where the averaging operator is defined by

$$\langle \zeta \rangle = \sqrt{\frac{2}{t_2 - t_1}\int_{t_1}^{t_2} \zeta^2\ dt}, \tag{34}$$

with t_1 and t_2 chosen to correspond to the final 30 tidal periods of each simulation. The phase is calculated from the zero-crossings of $U_{sim}(t)$ over the same time period. The phase of the benthic tide is reported as the phase difference from the flow at height (which is unaffected by topographic interactions), with a negative (positive) value denoting that the benthic flow leads (lags) the flow at height—consistent with the sign convention in the theory.

It was noted in Section 2, that the theoretical prediction for the benthic tide in the super-inertial regime is sensitive to the magnitude of the dissipation acting on the waves (i.e., the drag coefficient σ in Equation 24 depends on the Laplacian viscosities), and this is especially true when waves are near-resonant. Figure 2 shows
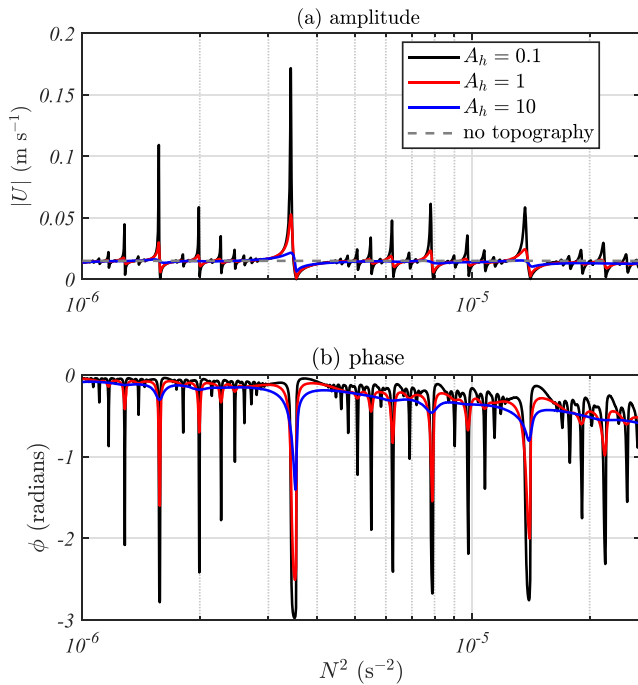
Figure 2. Amplitude and phase of bottom layer flow U predicted by Equation 25 for the abyssal hill topography as a function of buoyancy frequency N, for three different viscosities ($A_h = 0.1$, 1 and 10 m^{2}s^{-1}, and $A_z = A_h/100$). Super-inertial reference parameter values are used: $h_{rms} = 100$ m, $f = 10^{-4}$ s^{-1}, and $\omega = 1.3889 \times 10^{-4}$ s^{-1}.

the theoretical amplitude and phase of the benthic tide (i.e., Equation 25) as the (uniform) stratification is varied, for three different viscosities, with other parameters fixed to the reference values introduced above. Very large variations in both amplitude and phase occur near resonances (i.e., values of N for which integer multiplies of half-vertical-wavelengths fit into the ocean depth, for one of the permitted discrete horizontal wavenumbers $k = 2n_x\pi/L$). The amplitudes of these resonances are reduced by increased viscosity, which acts to dissipate waves and damp surface reflections. Strong amplification of the bottom flow is predicted when the vertical wavenumber is slightly less than the resonant wavenumber, and strong suppression when the vertical wavenumber is slightly larger. In both cases, the bottom flow is expected to significantly lead to the unperturbed flow at height.

In such near-resonant cases, the amplitude of the wave field will be large, and thus nonlinear wave breaking is likely to drive enhanced wave dissipation in the simulations. To account for such enhanced dissipation we introduce the concept of an "effective viscosity" for the waves. The minimum viscosity "seen" by the waves will be the explicit model viscosity; thus, we set the effective viscosity to be a factor M times the explicit viscosity, where $1 \leq M < \infty$. We call M the viscous magnification factor. In limit $M \to \infty$, there can be no reflections and the "strongly dissipative" limit studied by SAH is recovered. Here, we solve the theoretical problem for a range of M, to encompass the maximum possible spread in the theoretical solution for the benthic tide (i.e., the variation shown in Figure 2). This approach will allow calculation of a best fit solution which minimizes the difference between the theoretical prediction and the simulations; that is, minimizes the error function $E(M) = (U^{theory}(M) - U^{sim})^2$. We will show below that the best-fit M scales with the amount of wave dissipation in the numerical model.

4. Results

Snapshots of the model u velocity are shown in Figure 3 for the reference sub- and super-inertial runs. A deceleration of the flow near the topography is clearly visible in the sub-inertial case (Figure 3a), but any changes that exist in the super-inertial case (Figure 3b) are obscured by the presence of large amplitude internal tides. Internal tides corresponding to the second harmonic are also visible in the subinertial case, but only with low amplitude (note that these waves are neglected in our theory, which is formulated in the small-excursion limit). The equilibration of the spatial-mean flows is shown in Figures 3c and 3d. The subinertial mean flow equilibrates within a few tidal periods, whereas the super-inertial flow takes ∼200 periods since it relies on the reflection and dissipation of the propagating internal wave field.

We now compare the simulations to the theoretical predictions, starting with the subinertial cases.

4.1. Sub-inertial Flow

Figure 4a shows the mean flow magnitude ($\langle \overline{u}^x \rangle$ in solid black, and volumetric mean $\langle \overline{u}^{vol} \rangle$ in dashed black) from the reference numerical model run. The theoretical solution (red dashed line) accurately predicts the volumetric mean flow below the crest of the topography. Furthermore, as anticipated, the mean flow above the crest is unaffected by the presence of the topography (it exactly matches the red dotted "no topography" line). The subcrest flow slows down by 24% relative to the flow at height, which leads to an overall 2% slowdown in the depth-integrated (barotropic) flow. The same structure of the vertical profiles is observed for all sub-inertial simulations. Figure 4b compares the theoretical below-crest mean velocity modulus with the simulation value for six different sub-inertial runs. The agreement is excellent, even in cases where the drag is large (e.g., 2h and 3N runs) and velocity is reduced by up to 40% (beyond the limits of validity for the linear theory, which assumes the change in velocity due to the drag is small). We observe that the simulation with an exponential N^2 profile (cyan triangle on Figure 4b) has an identical sub-crest tidal flow to the
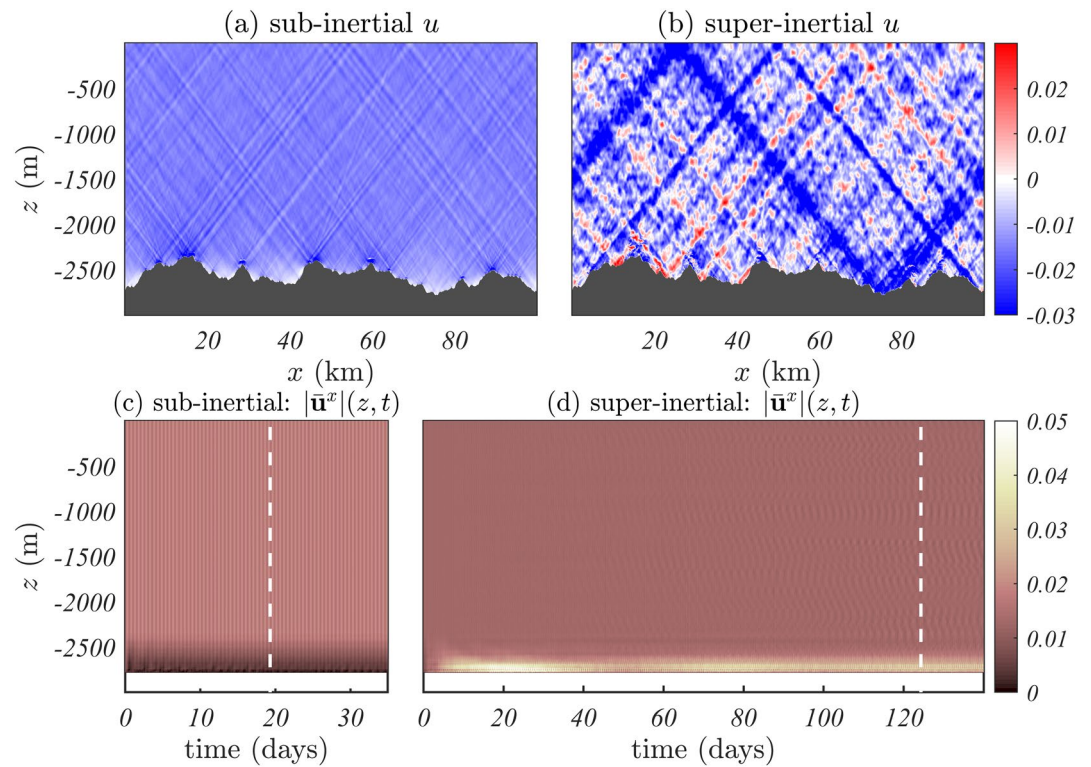
Figure 3. Snapshots of u velocity for the reference (a) subinertial (32 days after initialization), (b) super-inertial simulations (130 days after initialization). Spatial mean flow speed with time and depth for the reference (c) subinertial and (d) super-inertial simulations. The subinertial response establishes almost instantly, whereas the super-inertial response takes many tidal periods to equilibrate. The vertical white dashed line denotes the start of the final 30 tidal periods time-averaging used to compute results in subsequent sections.

reference case; that is, as predicted by Equation 28, the topographic stress in the sub-inertial limit depends only on the bottom stratification, and not the stratification at height. The sub-crest V velocity remains 90° out of phase with U (to within 0.01 radians) and with an amplitude of $V = Uf/\omega$, as predicted by theory (Figures 5a and 5b). The bottom flow also exhibits a small (≤2°) lag compared to the flow at height (Figure 5b), in comparison to the theoretical prediction of zero phase difference.

The flow prediction of the Jayne and St. Laurent (2001) parameterization (currently used in many global circulation models; GCMs) is also displayed in Figure 4b for each simulation in the sub-inertial regime (gray symbols). We observe that this parameterization significantly (by up to 50%) underestimates the damping of the flow by the topographic spring forces (which it parameterizes as dissipate drag forces). Clearly, there is a need to improve the current parameterization in GCMs, as we reflect on further in Section 5.

Figure 6 shows the mean bottom flow magnitude for simulations with increasing body forcing up to 5 times the reference value (yielding tidal flow speeds at a height of 7.5 cm/s). The theory predicts a 24% slow-down in the bottom flow (compared with the free stream flow at height) in all cases. However, as the forcing increases, the theory begins to overestimate the stress: the observed slow-down at the highest forcing (5F) is only 17% (Figure 6b).

4.2. Super-inertial Flow

Figure 7 compares the bottom layer velocity in the numerical simulations with super-inertial forcing to that calculated from theory. The vertical profile of mean flow for the reference (100 m rms height) run is shown in Figure 7a; this is a case where the below-crest mean flow is amplified by the presence of topography. The flow speed is more than doubled at depth in between the hills, with the volume-averaged below-crest flow increasing by 2 mm s^{-1} (~13%). Figures 7b and 7c display the corresponding volume averaged sub-crest
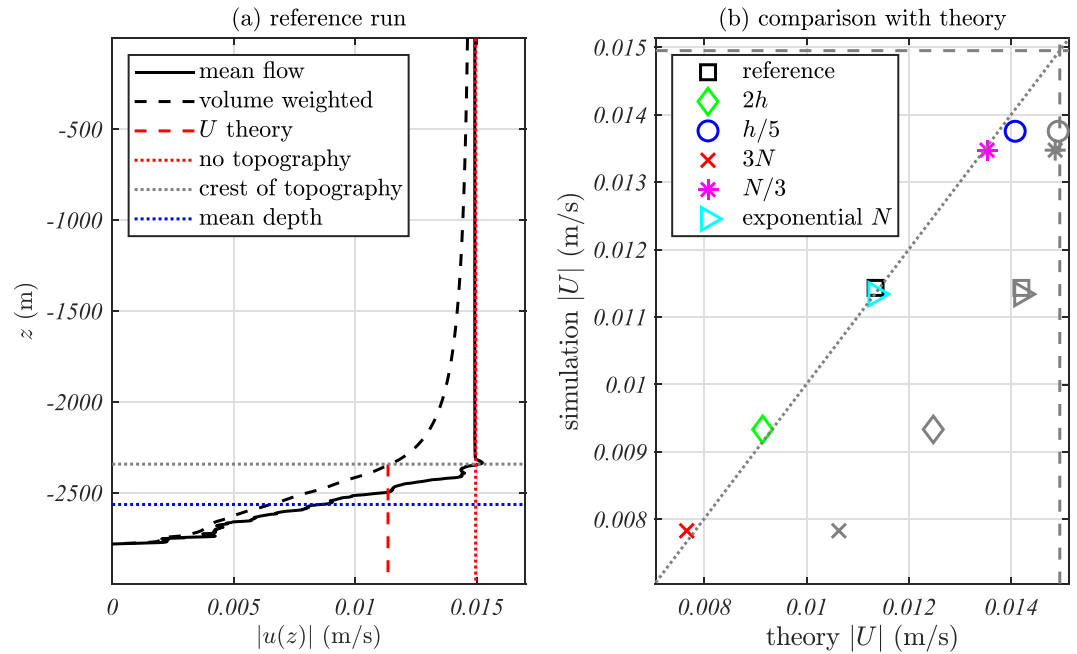
Figure 4. Results for sub-inertial forcing. (a) The horizontal mean flow magnitude from the reference simulation ($\langle \overline{u}^x \rangle$ in solid black; volumetric mean $\langle \overline{u}^{vol} \rangle$ in dashed black) and the theoretical predictions (red). The horizontal dotted lines show the mean-depth (lower; blue) and the crest of the topography (upper; gray). The theory precisely predicts the volumetric mean flow up to the crest of topography. (b) Comparison of theoretical prediction with numerical simulation for each sub-inertial run. The 1:1 line is shown (dotted), as is the flow magnitude in the absence of topography (dashed). Grayed symbols show the flow prediction of the JSL parameterization currently used in many baroclinic tide models: JSL significantly underestimates the decrease in benthic flow speeds induced by the topography.

U flow compared with theory for ten super-inertial simulations with different parameter values. The sub-crest V velocity in the super-inertial simulations remains 90° out of phase with U and with an amplitude of $V = Uf/\omega$, as predicted by theory (Figures 5c and 5d; the one exception is the simulation with enhanced viscosity ($3N$, $10A_h$; green triangle), where V is ~20% larger than expected). Amplitudes are observed to increase by up to 30% (resonant) and decrease by up to 30% ($2h$, $3N$), with phases leading by up to 10% of a period (0.6 radians) in the most extreme case ($2h$, $3N$). The horizontal errorbars in the figure show the range of possible values for the theoretical sub-crest flow as the dissipation amplification factor M is varied from $1 \le M < \infty$. The $M = 1$ value is shown by the colored marker and $M \to \infty$ value (where the stress is defined by Equation 29) by the gray circle. The range of theoretical values is consistent with the numerical results except for the four runs with elevated stratification ($3N$), where the flow amplitude is underestimated by ~20%. The best-fit flow magnitudes and phases—based on minimizing the error function $E(M) = (| U^{theory}(M) | - | U^{sim.} |)^2$)as explained in Section 3—are shown by black "+"s (the best-fit M value is given in the plot legend). Since the error function does not involve the phase, the match between the phase of the best-fit solution and the simulation (Figure 7c) provides an independent test of whether the viscous amplification model is physically meaningful. The agreement in the phase is generally improved in the best-fit solutions compared with $M = 1$, but remains poor for the resonant and ($2h$, $3N$) simulations. Taking the strongly dissipative limit (gray circles) also provides a comparably good measure of the benthic flow phase and amplitude for cases where the benthic flow is reduced—however, it fails for the resonant cases where the benthic flow is amplified. Nonetheless, the advantage of this approach is that there is no tuning parameter (i.e., factor M) and it depends only on the bottom stratification, making it more practical to use in developing a parameterization (as we discuss in more detail in Section 5).

In the cases discussed above, many different physical parameters are varying, and thus is hard to predict how viscous amplification M should vary between the solutions. To provide a clearer test of the best-fit methodology, we now consider a set of simulations where the body forcing F is increased, but with the other parameters held at the reference values (see Table 2). The time mean dissipation for each simulation
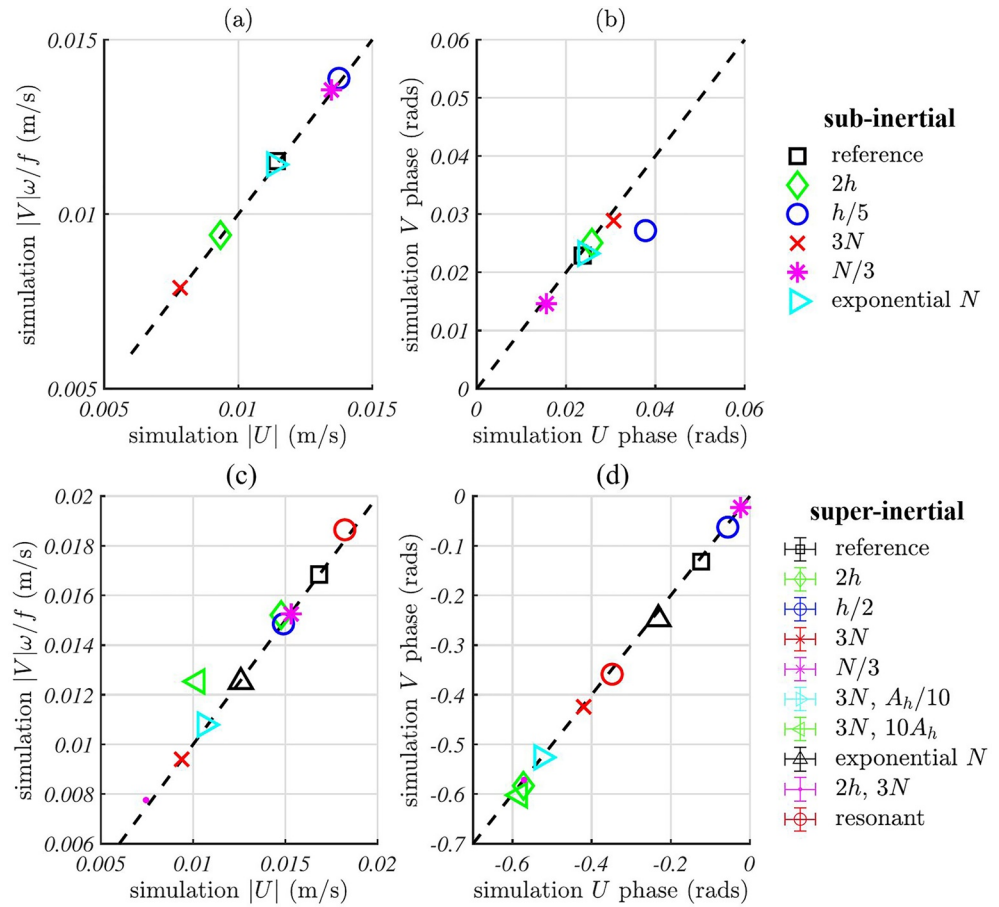
Figure 5. Comparison of benthic U and V velocities in the simulations with (a and b) sub- and (c and d) super-inertial forcing: (a and c) amplitude, and (b and d) phase relative to flow at height.

is shown in Figure 8. The structure of the dissipation varies considerably with increasing forcing. For the reference value (Figure 8a), enhanced dissipation is observed along wave ray paths (associated with linear dissipation by the explicit model viscosity), with some enhanced dissipation near the topography. As forcing increases, this near-topography layer of enhanced dissipation deepens, and turbulent dissipation is observed throughout the water column. Despite these changes to the dissipation profile (Figure 8f) with increasing forcing, the impact of the wave-induced topographic stress on the mean flow is felt over the same sub-crest layer (Figure 8g); that is, the location of the wave dissipation does not affect the *location* where topographic stresses act on the mean flow. This result is consistent with our theory. However, wave dissipation does affect the *magnitude* of the subcrest tidal flow.

Figure 9a shows the sub-crest tidal flow magnitude for each of the simulations with varying super-inertial body forcing. Even at the highest forcing ($5F$), the bottom flow is still amplified compared to the flow aloft. However, the relative amplification of the bottom flow is gradually reduced as forcing increases, from 13% amplification in the reference case to only 3% in the $5F$ case. The best-fit values for the viscous amplification M (black "+"s on Figure 9a) scale linearly with the depth-integrated dissipation above the crest of the topography, as shown in Figure 9b. Thus, the reduced deep tidal flow amplification with increasing forcing can be attributed to enhanced dissipation of the wave field. Both the simulations and theory show little variation in the phase of the sub-crest flow with changing forcing ($\phi = 0.1 \pm 0.1$ rads for all cases, or about 0%–4% of a tidal period; not shown).

It is instructive to consider the role of different topographic scales in controlling the sub-crest flow in the super-inertial regime. As pointed out by SAH, the real part of the drag coefficient for propagating waves scales with the wavenumber (i.e., smaller scales have a bigger effect), whereas the imaginary (resonant/reflective)
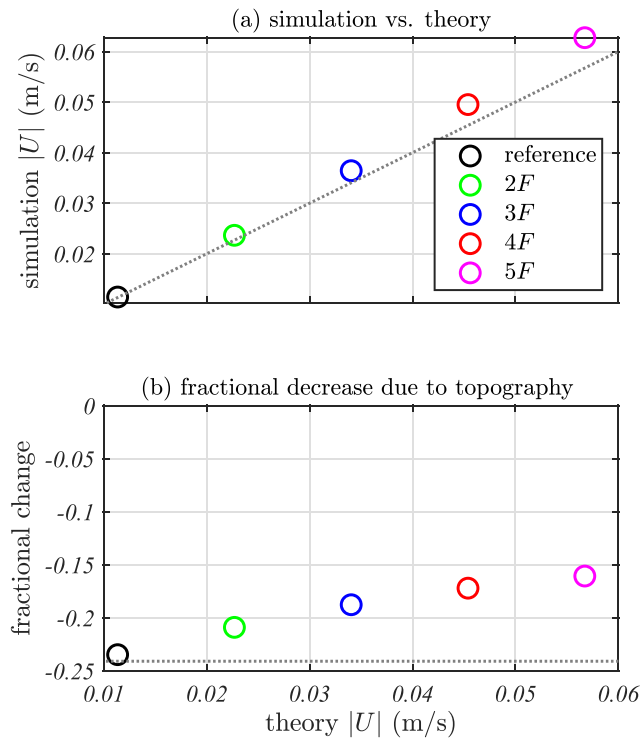
Figure 6. (a) Comparison of theory and simulation bottom flow speed for varying strength of the sub-inertial body forcing from one to five times the reference value. The 1:1 line is shown (dotted). (b) The fractional slow-down in the volumetric mean bottom flow compared with the flow at height (without topography). The theoretical slow-down is the same in all cases (dotted line, 24%).

part is largely independent of wavenumber (only the height of the topography matters). Since larger scales have greater rms heights, it follows that the resonant effect should be larger at larger scales. In order to separate these two effects, we decompose our 200m rms height topography into its small-scale rough part (wavelengths less than 10 km) and its large-scale smooth part (wavelengths exceeding 10 km)—and re-run the numerical model with these individual topographies. We also run a simulation with an extended 10 km-high domain, and a viscous sponge over the top 7 km to prevent reflections of internal tides from the ocean surface. Snapshots of the deep stratification in each simulation are shown in Figure 10. Overturning is present near the topography in all cases but is more pronounced in the combined and sponge cases (Figures 10a and 10c). Intriguingly, the only case that exhibits overturning at a significant height above the topography is the smooth simulation (e.g., near $x = 10$ km and $z = -1,400$m in Figure 10b).

The vertical profiles of the tidal flow amplitude for each of the four cases are shown in Figure 11a. We note that while the mean depth (gray dotted line) is the same in all cases, the crest heights are different (colored dotted lines). The smooth case has an amplified sub-crest flow, and strong sensitivity to the magnitude of dissipation (long horizontal error bar in Figure 11b), indicating the dominance of spring forces associated with large-scale wave reflections and resonance. By contrast, the rough case has a decreased subcrest flow and little sensitivity to dissipation (short horizontal error bar in Figure 11b). The "sponge" simulation is very similar to the rough case, with a decreased sub-crest flow. In both rough and sponge cases, the reflection of the large scales is absent: in one case because the topographic scales themselves are absent, and in the other, because the reflections from those scales are prevented. Without these large-scale reflections, the wave drag forces dominate over spring forces, and the benthic flow is damped. The real and imaginary parts of the drag coefficient from the best-fit theoretical solutions (cumulatively summed from small to large wavenumber) are shown in Figures 11c and 11d for each case. In the combined case (in green), all the imaginary drag is from large (>10 km) scales. Thus, the smooth case is dominated by imaginary drag from these scales, and the rough case is dominated by real drag from the smaller scales. We note, however, that the rough case exhibits some imaginary drag at scales of 5–10 km which is not observed in the combined case. This effect is because the wave amplitude in the rough case is weaker than in the combined case, resulting in a smaller effective viscosity (the best-fit M is $\sim 10^3$ times smaller; see legend) and allowing smaller scale waves that dissipate in the combined case, to start reflecting back to the seafloor and inducing spring forces in the rough case. Nonetheless, these results support neglecting the reflecting wave spring force when parameterizing tidal forcing in global circulation models, since its larger scale means that it will be the first component to be resolved by the model (as we discuss in more detail in the subsequent section).

5. Discussion

At scales of 1–100 km the ocean floor is covered by rough bathymetry known as "abyssal hills." These features are often unresolved in large-scale ocean and tide models. Thus, an important question is how the presence of these features affects the larger-scale flow in the deep ocean, and in particular, the large-scale tide. Here, we have extended the work of SAH to develop a model that answers this question. Crucial to this endeavor is a new theory that describes the vertical structure of wave stresses, and in particular, shows that the tidal-frequency wave stress associated with the internal tide (that feeds back on the spatial-mean tidal flow) acts in the exponentially decaying diffusive boundary layer near the topography. Indeed, in all scenarios studied here involving finite height topography, the stress may be considered to act below the crest of the abyssal hills, independent of where wave dissipation is occurring (which varies significantly
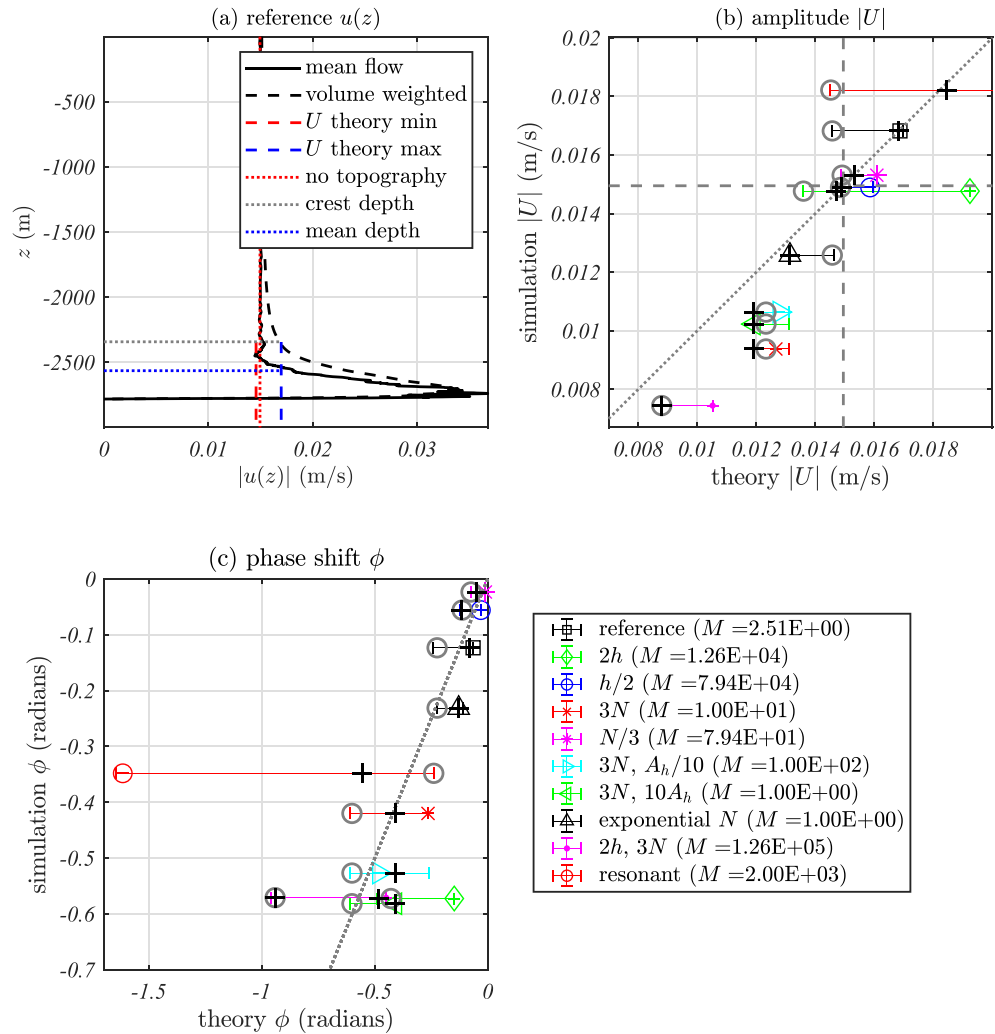
Figure 7. Results for super-inertial forcing. (a) The horizontal mean flow magnitude from the reference simulation ($\langle \overline{u}^x \rangle$ in solid black; volumetric mean $\langle \overline{u}^{vol} \rangle$ in dashed black) and the theoretical predictions (red and blue). The horizontal dotted lines show the mean-depth (blue) and the crest of the topography (gray). Comparison of theoretical prediction of U (b) amplitude and (c) phase shift with the numerical simulation for each super-inertial run. The 1:1 line is shown (dotted), as is the amplitude in the absence of topography (dashed). The horizontal error bars show the maximum and minimum possible values for varying viscous amplification factor $1 \le M < \infty$. The colored markers show the value for $M = 1$ (explicit model viscosity only). The gray circles show the value for $M \to \infty$. The black crosses show the best fit for M, with the best-fit value shown in the legend.

depending on the amplitude and nonlinearity of the wave field; e.g., Figure 8). This result illustrates the very significant difference of *time-periodic* internal tide wave stresses from *time-mean* internal lee wave stresses, which act where the lee waves dissipate. The reason for this distinction is that time-mean stresses that occur upon wave dissipation are associated with the deposition (upon dissipation) of the pseudo-momentum flux carried by the wave beam (e.g., Andrews & McIntyre, 1976), but for internal tides, this spatial-mean flux is zero owing to the equal and opposite nature of the generation of internal tide beams (Shakespeare, 2020; Shakespeare & Hogg, 2019). The action of the stress directly above the topography drives a spatial-mean tidal flow composed of two layers: an above-crest layer flow that does not "see" the topography, and a sub-crest layer flow that is modified by the topographic stresses. It is the flow in this sub-crest layer—which we have termed the "benthic tide"—that encounters the topography and therefore is responsible for generating internal tides. The topographic forces acting on the sub-crest layer modify subsequent internal tide generation. The depth-mean (or barotropic) flow is the height-weighted average of the two layers, $u_{bt} = (h_0/H) u_{sub} + ((H - h_0)/H) u_{above}$, and is thus much less influenced by the topographic stresses than the bottom
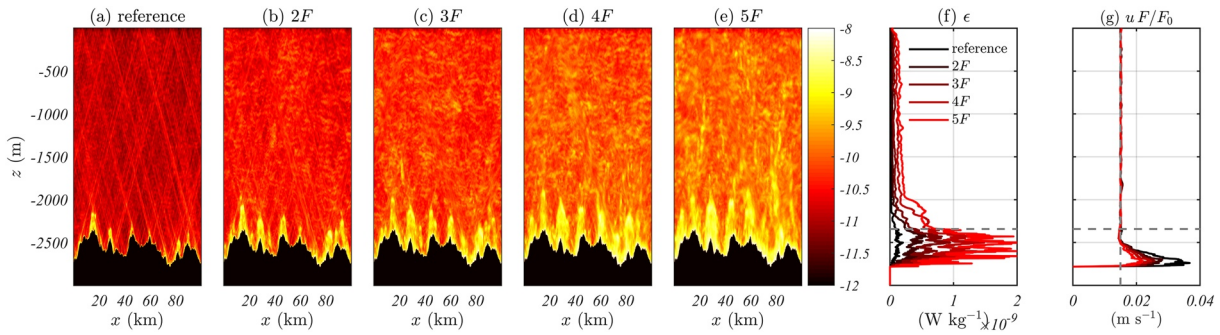
Figure 8. (a–e) Time-mean viscous dissipation (log10; W kg^{-1}) for super-inertial simulations with increasing body forcing F. The increasing non-linearity of the wave field as forcing increases is evident from the structure of the dissipation. (f) The horizontal average of (a–e). (g) The horizontal mean flow magnitude in each simulation (i.e., $\langle \overline{u}^x \rangle$), normalized by the forcing. The vertical dashed line shows the magnitude of the flow in the absence of topography, u_0. Horizontal dashed lines in (f and g) show the crest of the topography.

layer. For example, a 40% reduction in the subcrest flow equates to a 2% reduction in the barotropic flow for typical height scales (e.g., 200 m benthic layer in a 4 km deep ocean).

Our theoretical model predictions were validated against a suite of numerical simulations with varying tidal forcing, stratification, viscosity, and topography. We first looked at the change in the benthic tide associated with a sub-inertial tidal forcing. In these cases, the tidal flow at height drives nonpropagating, exponentially decaying motions directly above the topography. Unlike propagating internal tides, these bottom-trapped tides extract no energy from the spatial-mean tide. However, they do exert pressures that act to significantly damp the magnitude of the sub-crest spatial mean flow (by up to 40% in the cases considered here; Figure 4) without changing the phase. The theoretical model provides near-perfect predictions of the subcrest flow at
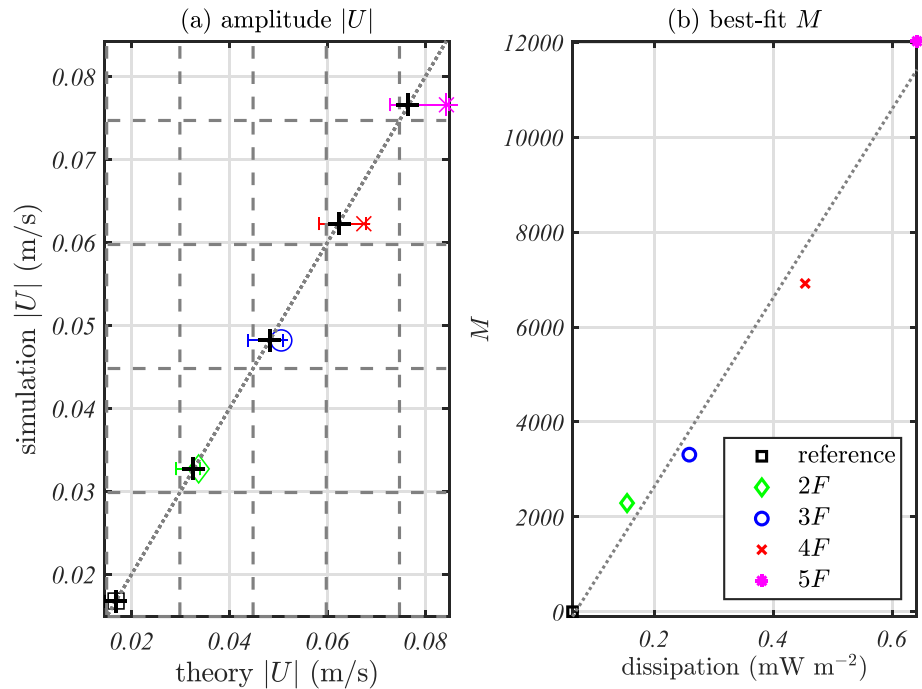

Figure 9. (a) Comparison of theory and simulation bottom flow speed for varying strength of the super-inertial body forcing from 1 to 5 times the reference value. The 1:1 line is shown (dotted), along with the unperturbed flow in each case (dashed). Colored markers show the theoretical solution with $M = 1$, errorbars show the range of possible solutions for $1 \leq M < \infty$, and black crosses the best-fit solution. The value of M for the best-fit solution is shown in (b); it increases linearly with the depth-integrated dissipation above the crest of topography (correlation coefficient is 0.99; line of best fit shown).
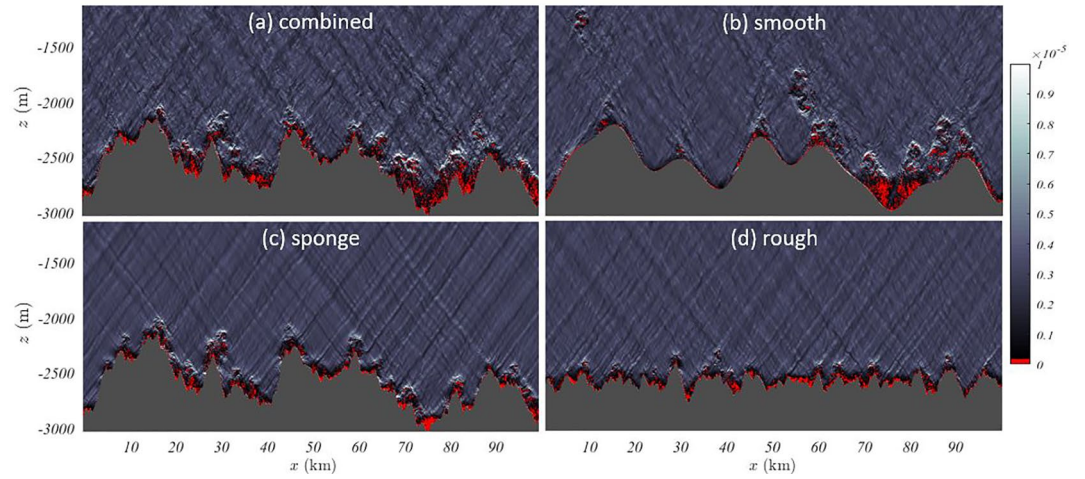
Figure 10. Snapshot of the stratification in the super-inertial numerical solutions for the (a) 2h, (b) 2h smooth (topographic scales exceeding 10 km only), (c) 2h with a 7 km deep viscous sponge at the top of the domain, and (d) 2h rough (topographic scales less than 10 km only).

realistic forcing (tidal flows of ~1.5 cm s^{-1}) but begins to break down at large forcing (tidal flows of >2 cm s^{-1}; Figure 6). The stress depends only on the properties of the topography and deep ocean stratification—it is independent of the ocean properties at height.

Second, we investigated the change in the benthic tide associated with a super-inertial tidal forcing that generates propagating internal tides. The topographic stress in this limit is associated with two distinct components: (i) an in-phase wave drag associated with the energy flux in the radiating internal tide, and (ii) an out-of-phase pressure associated with reflecting internal tides (the "spring force"). This second component
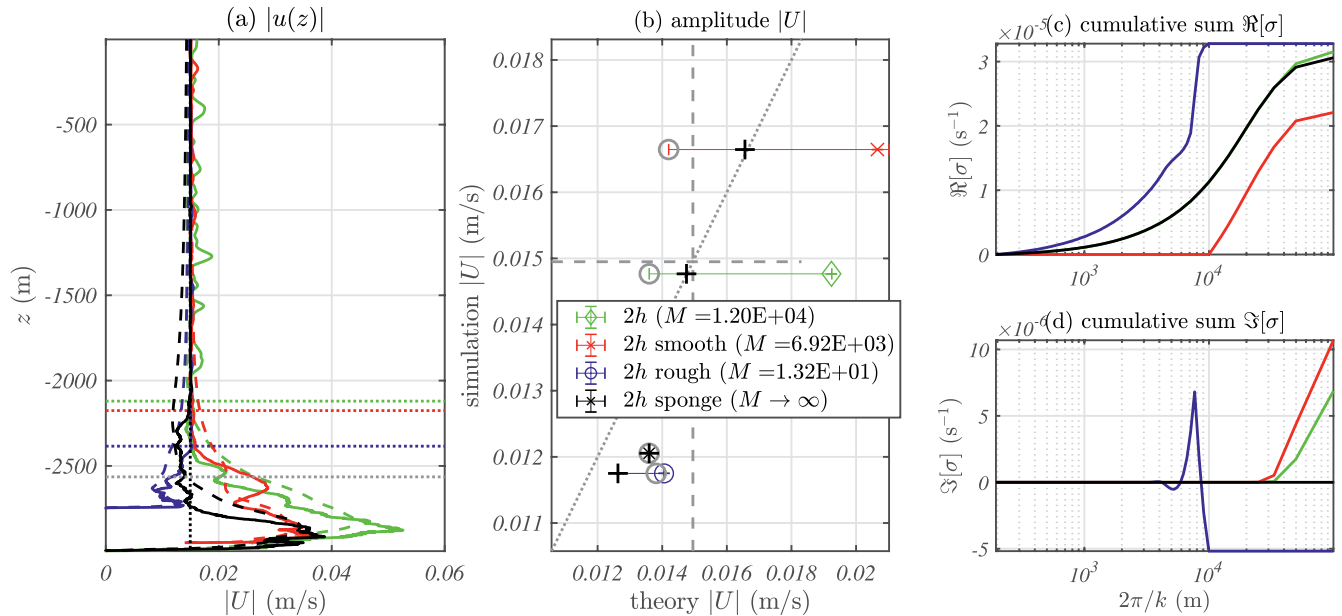

Figure 11. Results for combined (green), small-scale rough (blue), and large-scale smooth (red) topographies with super-inertial forcing. (a) The horizontal mean flow magnitude ($\langle \overline{u}^x \rangle$ in solid; volumetric mean $\langle \overline{u}^{vol} \rangle$ in dashed). The mean depth is shown by a gray line, and the crest of each topography by color dotted lines. (b) Comparison of theoretical prediction with numerical simulation. The 1:1 line is shown (dotted), as is the flow magnitude in the absence of topography (dashed). The horizontal errorbar shows the variation in theoretical solution as the viscosity is amplified by factor $1 \leq M \leq \infty$. The colored markers show the value for $M = 1$ (explicit model viscosity only). The gray circles show the value for $M \to \infty$. Black crosses show the best-fit solution with respect to M, with the best-fit value shown in the legend. (c) The real part of the drag coefficient for the best-fit solution. (d) The imaginary part of the drag coefficient for the best-fit solution.

is similar to the pressures exerted by bottom-trapped tides, but since it is associated with propagating and reflecting waves, unlike those pressures, its phasing is not fixed with respect to the spatial-mean tide but depends on the propagation path of the wave. Thus, these wave pressures can act to either decrease or amplify the sub-crest flow, depending on their phasing with respect to the tide at the reflection. In either case, since the force is out-of-phase with the tide, there is no time-mean energy exchange. Since these forces depend on the phasing of the internal tide, they are exceptionally sensitive to the details of the stratification (and presumably large-scale flows; e.g., eddies, jets) along the path of the waves, in addition to the strength of dissipation of the waves (since stronger dissipation implies less reflection), making them challenging to predict even in the idealized 2D simulations employed here (e.g., the theory is unable to precisely represent some of the super-inertial simulation results; e.g., Figure 7b). In some cases studied here (e.g., Figure 7) the sub-crest tidal flow is *amplified* by 30% compared with the flow at height. We also verified SAH's prediction that the wave pressures (spring force) are dominated by larger scale topography, whereas the wave drag forces are dominated by smaller-scale topography (Figure 11). It remains to be investigated how the reflecting internal tide spring force is modified in more complex three-dimensional eddying flows.

We now consider how our results may be applied in developing topographic stress parameterizations for baroclinic tide models. One key result is that the topographic stresses act in the diffusive boundary layer directly above the topography, where time-mean isopycnals are tilted to satisfy the zero buoyancy flux bottom boundary condition. This result confirms that topographic stress parameterizations should be applied in the bottom (or bottom few) layers of numerical models—which are typical of O(100)m depth—as is already done in most cases (e.g., Ansong et al., 2015; Arbic, Richman, et al., 2012, 2010). A second key result is that the spring forces associated with bottom-trapped tides generated at abyssal hills have a significant and predictable impact on the deep-ocean tidal flow, but are not included in any currently used topographic stress parameterization. Indeed, current parameterizations such as Jayne and St. Laurent (2001, JSL) impose a propagating wave drag in such locations (poleward of critical latitudes) which is inconsistent with the dynamics and leads to significant errors. For example, Figure 4 shows the benthic flow predicted by JSL compared with our simulation results: JSL overestimates the flow speed (or equivalently, underestimates the impact of the topographic forces) by up to 50% in these cases. The simplicity of the correct stress formulation (Equation 28) for bottom-trapped tides suggests that it would be straightforward to implement in baroclinic tide models. A third key result is that larger-scale (>10 km horizontal wavelength) reflecting internal tides create a topographic spring force that can very significantly increase or decrease the deep ocean spatial-mean tide, dependent on the resonant and dissipative properties of the system (i.e., the amplitude and phase of the reflection). This result is problematic from a parameterization perspective since it is near-impossible to predict the phase of the reflected wave through a realistic 3D ocean with varying stratification and mean flows. There is also the potential for the parameters characterizing the topography (i.e., the abyssal hill spectrum) to vary laterally, meaning that reflected waves encounter topography that is spectrally distinct from that which generated the waves, possibly damping the resonant effects described by the theory. The only realistic solution to these issues appears to be running a baroclinic tide model that resolves these scales. However, smaller-scale internal tides (<10 km horizontal wavelength) are dominated by frictional stresses which are largely insensitive to the details of reflections and can be readily parameterized. In the limit that reflections can be ignored, the internal tide drag coefficient reduces to

$$\sigma = \frac{1}{h_0} \frac{\sqrt{(N(-H)^2 - \omega^2)(\omega^2 - f^2)}}{|\omega|} \bar{k} h_{rms}^2, \tag{35}$$

identical in form to the bottom-trapped tide stress (i.e., Equation 28; except it is real, since $\omega > f$). We showed that using this purely real drag coefficient provides a reasonable estimate of the benthic flow even for simulations including larger scales (e.g., gray circles in Figure 7) as long as the simulations are not near a resonance, where the (neglected) spring forces are large. As shown by SAH, the extant JSL parameterization implements a nonfrequency dependent approximation (in the limit $f \ll \omega \ll N$) of Equation 35: $\sigma_{JSL} = h_0^{-1} N(-H) \bar{k} h_{rms}^2$. Based on our results, we recommend extending this parameterization to include the frequency dependence explicitly, and thus also incorporate both propagating internal tides (equatorward of critical latitudes) and nonpropagating bottom-trapped tides (poleward of critical latitudes).

6. Conclusions

We have presented the new theory that predicts the amplitude and vertical structure of the topographic stresses applied to an oscillating fluid encountering rough topography and validated this theory with idealized 2D numerical simulations with time-periodic body forcing. The presence of a rough seafloor can, unsurprisingly, lead to a reduction in the magnitude of the large-scale tide near the ocean bottom (the benthic tide), but here we have shown that the opposite can also be true: the presence of a rough seafloor can lead to an enhancement of the benthic tide, due to resonant reflections of internal tides. It remains to be determined whether the 3D form of the theory presented here will agree with fully 3D simulations of more realistic flows—a topic which is left to future work.

Data Availability Statement

Data are available via Zenodo at https://doi.org/10.5281/zenodo.4093543, and model configuration files are available at https://doi.org/10.5281/zenodo.4721932.

References

Adcroft, A., Anderson, W., Balaji, V., Blanton, C., Bushuk, M., Dufour, C. O., et al. (2019). The GFDL global ocean and sea ice model OM4.0: Model description and simulation features. *Journal of Advances in Modeling Earth Systems*, *11*(10), 3167–3211. https://doi.org/10.1029/2019ms001726

Andrews, D. G. (1983). A finite-amplitude Eliassen-palm theorem in isentropic coordinates. *Journal of the Atmospheric Sciences*, *40*(8), 1877–1883. https://doi.org/10.1175/1520-0469(1983)040<1877:afaept>2.0.co;2

Andrews, D. G., & McIntyre, M. E. (1976). Planetary waves in horizontal and vertical shear: The generalized Eliassen-Palm relation and the mean zonal acceleration. *Journal of the Atmospheric Sciences*, *33*(11), 2031–2048. https://doi.org/10.1175/1520-0469(1976)033<2031:pwihav>2.0.co;2

Andrews, D. G., & McIntyre, M. E. (1978). Generalized eliassen-palm and charney-drazin theorems for waves on axismmetric mean flows in compressible atmospheres. *Journal of the Atmospheric Sciences*, *35*(2), 175–185.

Ansong, J. K., Arbic, B. K., Buijsman, M. C., Richman, J. G., Shriver, J. F., & Wallcraft, A. J. (2015). Indirect evidence for substantial damping of low-mode internal tides in the open ocean. *Journal of Geophysical Research: Oceans*, *120*(9), 6057–6071. https://doi.org/10.1002/2015jc010998

Arbic, B., Richman, J., Shriver, J., Timko, P., Metzger, J., & Wallcraft, A. (2012). Global modeling of internal tides within an eddying ocean general circulation model. *Oceanography*, *25*(2), 20–29. https://doi.org/10.5670/oceanog.2012.38

Arbic, B. K., Alford, M. H., Ansong, J. K., Buijsman, M. C., Ciotti, R. B., Farrar, J. T., et al. (2018). Primer on global internal tide and internal gravity wave continuum modeling in hycom and mitgcm. *New Frontiers in Operational Oceanography*, 307–392. https://doi.org/10.17125/gov2018.ch13

Arbic, B. K., Wallcraft, A. J., & Metzger, E. J. (2010). Concurrent simulation of the eddying general circulation and tides in a global ocean model. *Ocean Modelling*, *32*(3–4), 175–187. https://doi.org/10.1016/j.ocemod.2010.01.007

Bell, T. H. (1975). Topographically generated internal waves in the open ocean. *Journal of Geophysical Research*, *80*(3), 320–327. https://doi.org/10.1029/jc080i003p00320

Bölöni, G., Ribstein, B., Muraschko, J., Sgoff, C., Wei, J., & Achatz, U. (2016). The interaction between atmospheric gravity waves and large-scale flows: An efficient description beyond the nonacceleration paradigm. *Journal of the Atmospheric Sciences*, *73*(12), 4833–4852. https://doi.org/10.1175/jas-d-16-0069.1

Boyd, J. P. (1976). The noninteraction of waves with the zonally averaged flow on a spherical earth and the interrelationships on eddy fluxes of energy, heat and momentum. *Journal of the Atmospheric Sciences*, *33*(12), 2285–2291. https://doi.org/10.1175/1520-0469(1976)033<2285:tnowwt>2.0.co;2

Bretherton, F. P. (1969). Momentum transport by gravity waves. *Quarterary Journal of Royal Meteorological Society*, *95*(404), 213–243. https://doi.org/10.1002/qj.49709540402

Charney, J. G., & Drazin, P. G. (1961). Propagation of planetary-scale disturbances from the lower into the upper atmosphere. *Journal of Geophysical Research*, *66*(1), 83–109. https://doi.org/10.1029/jz066i001p00083

Egbert, G. D., & Erofeeva, S. Y. (2002). Efficient inverse modeling of barotropic ocean tides. *Journal of Atmospheric and Oceanic Technology*, *19*(2), 183–204. https://doi.org/10.1175/1520-0426(2002)019<0183:eimobo>2.0.co;2

Egbert, G. D., Ray, R. D., & Bills, B. G. (2004). Numerical modeling of the global semidiurnal tide in the present day and in the last glacial maximum. *Journal of Geophysical Research*, *109*(C3). https://doi.org/10.1029/2003jc001973

Eliassen, A., & Palm, E. (1961). On the transfer of energy in stationary mountain waves. *Geofysiske Publikasjoner*, *22*, 1–23.

Falahat, S., & Nycander, J. (2015). On the generation of bottom-trapped internal tides. *Journal of Physical Oceanography*, *45*(2), 526–545. https://doi.org/10.1175/jpo-d-14-0081.1

Garner, S. T. (2005). A topographic drag closure built on an analytical base flux. *Journal of the Atmospheric Sciences*, *62*(7), 2302–2315. https://doi.org/10.1175/jas3496.1

Goff, J. A. (1991). A global and regional stochastic analysis of near-ridge abyssal hill morphology. *Journal of Geophysical Research*, *96*(B13), 21713–21737. https://doi.org/10.1029/91jb02275

Goff, J. A. (2010). Global prediction of abyssal hill root-mean-square heights from small-scale altimetric gravity variability. *Journal of Geophysical Research*, *115*(B12). https://doi.org/10.1029/2010jb007867

Goff, J. A., & Arbic, B. K. (2010). Global prediction of abyssal hill roughness statistics for use in ocean models from digital maps of paleo-spreading rate, paleo-ridge orientation, and sediment thickness. *Ocean Modelling*, *32*(1–2), 36–43. https://doi.org/10.1016/j.ocemod.2009.10.001

Goff, J. A., & Jordan, T. H. (1988). Stochastic modeling of seafloor morphology: Inversion of sea beam data for second-order statistics. *Journal of Geophysical Research*, *93*(B11), 13589–13608. https://doi.org/10.1029/jb093ib11p13589

Green, J. A. M., & Nycander, J. (2013). A comparison of tidal conversion parameterizations for tidal models. *Journal of Physical Oceanography*, *43*(1), 104–119. https://doi.org/10.1175/jpo-d-12-023.1

Jayne, S. R., & St Laurent, L. C. (2001). Parameterizing tidal dissipation over rough topography. *Geophysical Research Letters*, *28*(5), 811–814. https://doi.org/10.1029/2000gl012044

Kelly, S., & Nash, J. (2010). Internal-tide generation and destruction by shoaling internal tides. *Geophysical Research Letters*, *37*(23). https://doi.org/10.1029/2010gl045598

Kelly, S., Nash, J., & Kunze, E. (2010). Internal-tide energy over topography. *Journal of Geophysical Research*, *115*(C6). https://doi.org/10.1029/2009jc005618

Llewellyn Smith, S. G., & Young, W. R. (2002). Conversion of the barotropic tide. *Journal of Physical Oceanography*, *32*(5), 1554–1566. https://doi.org/10.1175/1520-0485(2002)032<1554:cotbt>2.0.co;2

Marshall, J., Adcroft, A., Hill, C., Perelman, L., & Heisey, C. (1997). A finite-volume, incompressible Navier Stokes model for studies of the ocean on parallel computers. *Journal of Geophysical Research*, *102*(C3), 5753–5766. https://doi.org/10.1029/96jc02775

Nelson, A., Arbic, B., Menemenlis, D., Peltier, W., Alford, M., Grisouard, N., & Klymak, J. (2020). Improved internal wave spectral continuum in a regional ocean model. *Journal of Geophysical Research: Oceans*, *125*(5), e2019JC015974. https://doi.org/10.1029/2019jc015974

Rocha, C. B., Gille, S. T., Chereskin, T. K., & Menemenlis, D. (2016). Seasonality of submesoscale dynamics in the Kuroshio extension. *Geophysical Research Letters*, *43*(21), 11–304. https://doi.org/10.1002/2016gl071349

Shakespeare, C. J. (2020). Interdependence of internal tide and lee wave generation at abyssal hills: Global calculations. *Journal of Physical Oceanography*, *50*, 655–677. https://doi.org/10.1175/JPO-D-19-0179.1

Shakespeare, C. J., Arbic, B. K., & McC. Hogg, A. (2020). The drag on the barotropic tide due to the generation of baroclinic motion. *Journal of Physical Oceanography*, *50*, 3467–3481. https://doi.org/10.1175/JPO-D-19-0167.1

Shakespeare, C. J., Arbic, B. K., & Hogg, A. McC. (2021). Dissipating and reflecting internal waves. *Journal of Physical Oceanography*, https://doi.org/10.1175/JPO-D-20-0261.1

Shakespeare, C. J., & Hogg, A. M. (2017). The viscous lee wave problem and its implications for ocean modeling. *Ocean Modelling*, *113*, 22–29. https://doi.org/10.1016/j.ocemod.2017.03.006

Shakespeare, C. J., & Hogg, A. M. (2019). On the momentum flux of internal tides. *Journal of Physical Oceanography*. https://doi.org/10.1175/JPO-D-18-0165.1

Wang, J., Fu, L.-L., Qiu, B., Menemenlis, D., Farrar, J. T., Chao, Y., et al. (2018). An observing system simulation experiment for the calibration and validation of the surface water ocean topography sea surface height measurement using in situ platforms. *Journal of Atmospheric and Oceanic Technology*, *35*(2), 281–297. https://doi.org/10.1175/jtech-d-17-0076.1

Winters, K. B., & Armi, L. (2014). Topographic control of stratified flows: Upstream jets, blocking and isolating layers. *Journal of Fluid Mechanics*, *753*, 80–103. https://doi.org/10.1017/jfm.2014.363

Xie, J.-H., & Vanneste, J. (2017). Interaction between mountain waves and shear flow in an inertial layer. *Journal of Fluid Mechanics*, *816*, 352–380. https://doi.org/10.1017/jfm.2017.39

Zaron, E. D., & Egbert, G. D. (2006). Estimating open-ocean barotropic tidal dissipation: The Hawaiian ridge. *Journal of Physical Oceanography*, *36*(6), 1019–1035. https://doi.org/10.1175/jpo2878.1